ACS APPLIED MATERIALS & INTERFACES

Research Article

Cite This: ACS Appl. Mater. Interfaces 2019, 11, 36316−36323

www.acsami.org

Colorimetric Sensor Array for Human Semen Identification Designed by Coupling Zirconium Metal−Organic Frameworks with DNA-Modified Gold Nanoparticles

Zhaowei Sun,[†] Shuai Wu,[†] Jiehua Ma,[†,‡] Hai Shi,[†] Lin Wang,[†] Anzhi Sheng,[§] Tingting Yin,[∥] Lizhou Sun,*[,∥] and Genxi Li*[,†,§]

[†]State Key Laboratory of Pharmaceutical Biotechnology, School of Life Sciences, Nanjing University, Nanjing 210023, P. R. China

[‡]State Key Laboratory of Reproductive Medicine, Department of Reproductive Health, Obstetrics and Gynecology Hospital Affiliated to Nanjing Medical University, Nanjing 210004, P. R. China

[§]Center for Molecular Recognition and Biosensing, School of Life Sciences, Shanghai University, Shanghai 200444, P. R. China

[∥]Department of Obstetrics and Gynecology, The First Affiliated Hospital of Nanjing Medical University, Nanjing 210036, P. R. China

Supporting Information

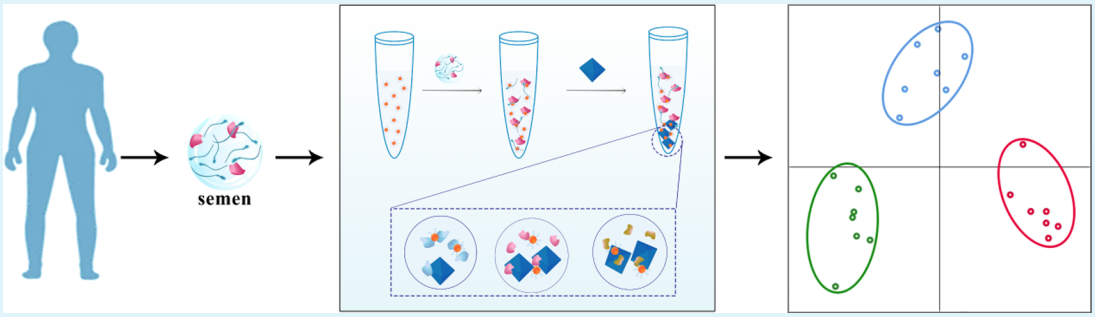

ABSTRACT: Rapid and accurate identification of semen is critical for male infertility diagnosis and the arrangement of personalized treatment. However, the complexity and diversity of samples impose lots of restrictions in detection. To solve this problem, we propose a colorimetric sensor array in this work by coupling zirconium metal−organic frameworks (Zr-MOFs) with single-stranded-DNA-decorated gold nanoparticles (ssDNA-AuNPs) for human semen identification. Because of the coordination interactions between the Zr_6 clusters and the DNA phosphate backbone, as well as $\pi-\pi$ stacking and H-bonding, Zr-MOFs can absorb and precipitate AuNPs with the aid of single-stranded DNA. What's more, addition of semen samples in the test solution, proteins, or other contents in the samples will affect the co-precipitation of Zr-MOFs and ssDNA-AuNPs. Subsequently, the color of the supernatant will change and a method to identify human semen can be developed. Further studies reveal that the method can completely detect different semen cases based on the differences in inclusions, demonstrating the characteristics of simplicity, feasibility, and sensitivity in the application of male infertility diagnosis.

KEYWORDS: *biosensor, male infertility, human semen, Zr-MOF, colorimetric assay*

1. INTRODUCTION

Infertility refers to the inability of a couple to become pregnant within a year, who are sexually active and do not take contraception. According to statistics, 15% of couples have such troubles, 50% of which are abnormalities in male semen parameters.[1,2] At present, semen analysis is mainly based on the World Health Organization guidelines, including analysis of the parameters such as sperm concentration, number, vitality, and morphology.[3] However, due to the lack of available data on semen variables in direct samples, the threshold for the normal range has not been clearly defined.[4] Moreover, there are still 30−45% infertility with abnormal semen parameters that have not yet been identified and the cases of these abnormalities are collectively referred to as idiopathic male infertility.[5] Therefore, there is an urgent need for a novel method to analyze the causes of male infertility and provide a reference for the arrangement of personalized treatments.

Semen is a heterogeneous composition, and it has been found that proteins are highly abundant molecules and constitute the main effectors of the functional interaction with spermatozoa.[6−11] Reported studies have identified 6198 different proteins in human sperm and seminal fluid proteome, which affect sperm maturation, sperm motility, as well as

Received: June 18, 2019
Accepted: September 16, 2019
Published: September 16, 2019

DOI: 10.1021/acsami.9b10729
ACS Appl. Mater. Interfaces 2019, 11, 36316−36323

Scheme 1. Illustration of (A) the Synthesis of UiO-66-NH_2 Nanoparticles and the Conjunction with DNA and (B) the Mechanism of the Colorimetric Sensor Array Strategy for Semen Sample Detection

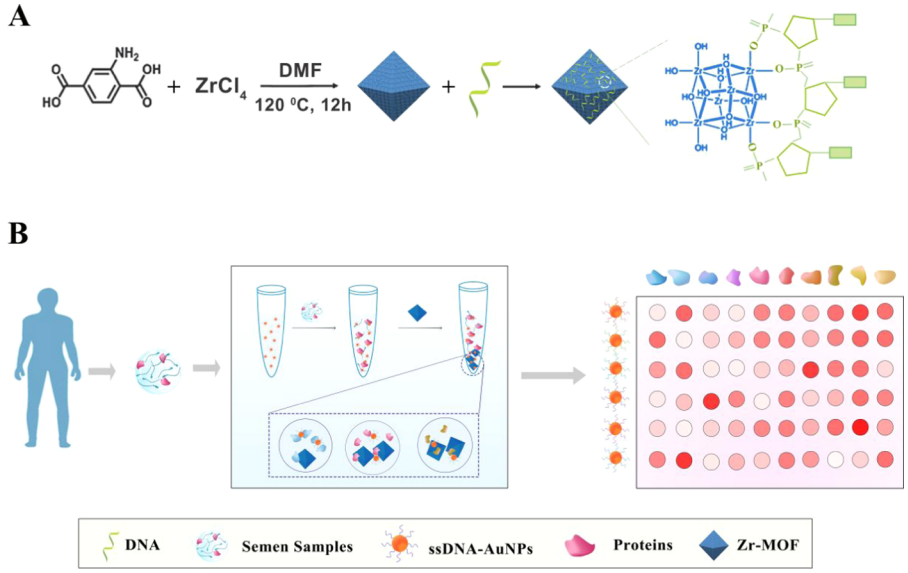

semen clot formation and liquefaction, such that 284 differential proteins involve in asthenozoospermia and 109 proteins influence human sperm motility.[12,13] Although the rapid and efficient detection of proteins plays an important role in many fields, many systems cannot perform multiple analyses simultaneously due to the limitations of specific binding interactions between proteins and receptors.[14−16] Currently, some techniques such as mass spectrometry and high-throughput proteomics technologies have been used to study the mechanisms of male infertility; however, they require specialized training and expensive equipment.[8,10,11] In particular, there are many restrictions to traditional detection methods because of the complexity and diversity of semen samples. Therefore, in consideration of the ever-increasing demands on medical diagnosis, rapid, simple, and sensitive methods of various protein analyses instead of a "lock−key" specific recognition strategy are highly demanded.

Herein, we have proposed a colorimetric sensor array in this work by coupling zirconium metal−organic frameworks (Zr-MOFs) with single-stranded-DNA-decorated gold nanoparticles (ssDNA-AuNPs) for the fast and accurate identification of human semen. As is illustrated in Scheme 1, six designed single-stranded DNA sequences are modified on the AuNP surface to form distinct sensor elements for array sensing.[17,18] UiO-66, a typical Zr-based porphyrinic MOF nanoparticle, can be successfully bound with oligonucleotides because of the interactions between the Zr_6 clusters and the DNA phosphate backbone.[19,20] Also, the MOF structure contains aromatic electron-rich ligands that can be combined with ssDNA via $\pi-\pi$ stacking and H-bonding.[21] Therefore, ssDNA-AuNPs can be bound and precipitated by Zr-MOFs, resulting in the lightening of the color of the supernatant. What is more, when different semen samples are added, some of the contents, such as proteins, will adsorb onto the surface of ssDNA-AuNPs by nonspecific binding, affecting the subsequent co-precipitation of Zr-MOFs and ssDNA-AuNPs.[22,23] The differential interactions between various contents in semen and ssDNA-AuNPs as well as MOFs will generate distinct colorimetric patterns. Therefore, we are able to easily discern different semen samples by recording the absorbance values of the supernatant before and after addition of semen samples. Notably, the color-based signal readout does not require the aid of any advanced instrument and the fabricated biosensor uses stable and cost-effective reagents, making this approach particularly suitable for point-of-care (POC) testing.

2. EXPERIMENTAL SECTION

2.1. Materials and Instrumentation. $ZrCl_4$, *N*,*N*-dimethylformamide (DMF), aminoterephthalic acid (NH_2-BDC), benzoic acid, tris(2-carboxyethyl)phosphine (TCEP), sodium citrate, horseradish peroxidase (HRP), lysozyme (Lys), myoglobin (Mb), transferrin (Tf), hemoglobin (Hem), cytochrome C (Cyto), concanavalin (Con), trypsin (Try), thrombin (Thr), and bovine serum albumin (BSA) were ordered from Sigma-Aldrich (Shanghai, China). $HAuCl_4 \cdot 3H_2O$ was purchased from Sinopharm Chemical Reagent Co. Ltd. (Shanghai, China). The 96-well plates were purchased from Sigma-Aldrich. All of the SH-labeled DNA sequences were synthesized and purified from Sangon Biotech (Shanghai, China). Other commercially available reagents were of analytical grade and were directly used without additional purification. The healthy human serum samples were obtained from Nanjing Second Hospital. The semen samples of healthy, infertile, and recurrent abortion cases were collected from Nanjing Maternity and Child Health Care Hospital.

Transmission electron microscopy (TEM) images were obtained by Tecnai G2 F20 S-TWIN with an accelerating voltage of 200 kV (FEI). Powder X-ray diffraction (PXRD) data of the sample was recorded by a D8 Advance diffractometer (Bruker, Germany). The absorption spectra of AuNPs were recorded by a UV-1800 spectrophotometer (Shimadzu, Japan) and Safire microplate Analyzer (Micromeritics ASAP2020). The ultrapure water used in this work was obtained from a Milli-Q system (Millipore, Bedford, MA).

2.2. Synthesis of UiO-66-NH_2. Zr-MOFs were prepared based on a previously reported method.[24] First, $ZrCl_4$ (120 mg), aminoterephthalic acid (110 mg), and benzoic acid (1.9 g) were dissolved in 10 mL of DMF and transferred to a Teflon liner. After 3 min of sonication, the mixture was reacted without stirring at 120 °C for 24 h. Then, the resulting product was obtained by centrifugation and washed repeatedly with fresh DMF and methanol (8000 rpm, 5 min). Finally, to remove the residual organic solvents, the nanoparticles were collected after drying overnight at 65 °C.

2.3. Preparation of Gold Nanoparticles. AuNPs (15 nm) were prepared by reduction of $HAuCl_4$ solution with sodium citrate.[25] Briefly, when the $HAuCl_4$ solution (50 mL, 1 mM) was heated to

DOI: 10.1021/acsami.9b10729
ACS Appl. Mater. Interfaces 2019, 11, 36316−36323

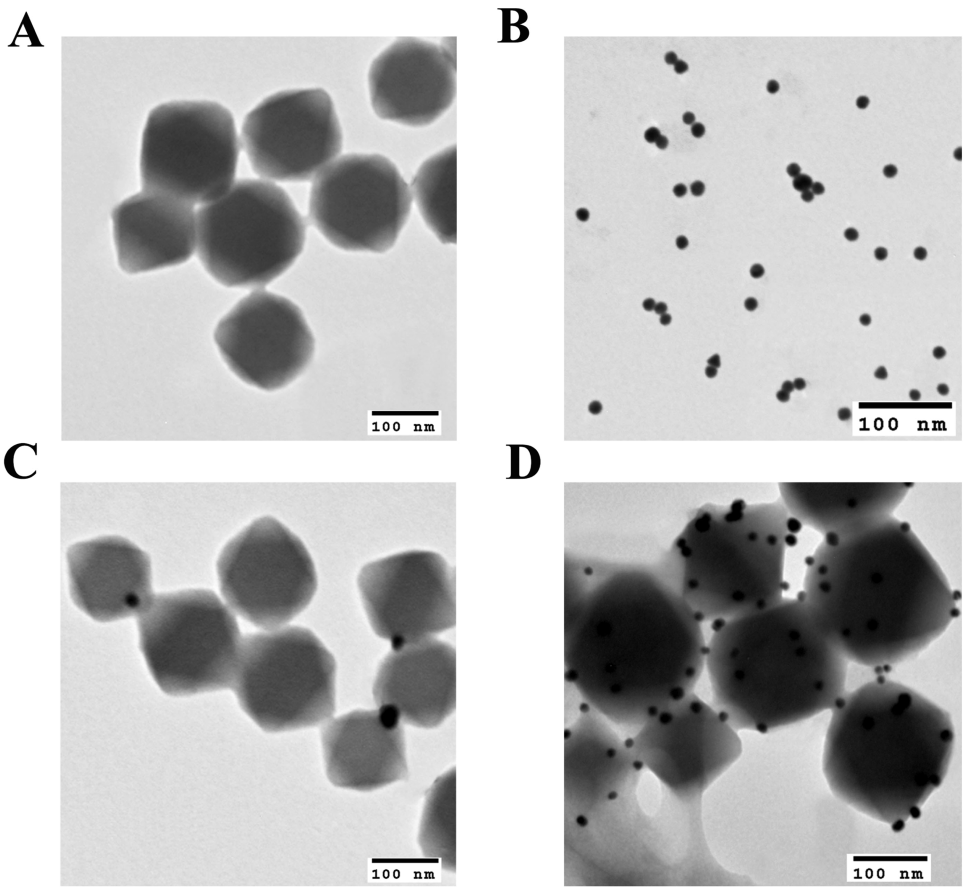

Figure 1. TEM images of (A) Zr-MOFs, (B) AuNPs, (C) Zr-MOFs incubated with AuNPs, and (D) Zr-MOFs incubated with ssDNA−AuNPs.

boiling, trisodium citrate solution (5 mL, 38.8 mM) was quickly added under vigorous stirring. The mixed solution was continuously heated and thoroughly stirred for another 30 min to ensure the completion of the reaction. After cooling down, the dark red solution was stored at 4 °C for use. The concentration of AuNPs was calculated according to the Beer−Lambert law.[26] The modification of AuNPs with thiolated DNA was achieved according to a previous method.[27] Before the DNA−AuNP conjugate, the DNA strand was activated by TCEP (10 mM) for 1 h and then incubated with as-prepared AuNP colloidal solution for 16 h (the DNA final concentrations is 3 μM). After that, 0.1 M NaCl was added dropwise to the mixture for "ageing" and incubation was continued for another 24 h. Subsequently, the solution was centrifuged and washed at 13 000 rpm for 30 min to remove the excess DNA in the supernatant. Finally, the red oily precipitate was dispersed in 1 mL of Tris−HCl buffer solution (20 mM Tris−HCl buffer with 100 mM NaCl at pH 7.4).

2.4. Sensing Studies. To facilitate the accurate performance of the array-based sensor, ssDNA-AuNPs (NP1−NP6) and Zr-MOFs were diluted with Tris−HCl buffer to the final concentrations of 3.5 nM and 100 μg/mL respectively. In a 96-well microplate, each of the ssDNA-AuNPs (60 μL) was respectively pipetted into each well and the absorption intensities (A_0) of the solutions were recorded by a Safire microplate reader at 521 nm. Then, different analytes (20 μL) were added under 30 min of incubation. After the combination finished, the mixture solution was introduced (30 μL of Zr-MOFs) for another 2 h to conjugate and precipitate the remaining ssDNA-AuNPs or analytes. The supernatants without precipitation were carefully pipetted into a new 96-well microplate, and the absorption intensities (A) were measured. The relative absorption intensity variation ($A_0 - A$) of each analyte was used as the absorbance response. Finally, the raw data matrix was processed by linear discriminant analysis (LDA) treatment in SPSS v25.0.

3. RESULTS AND DISCUSSION

3.1. Characterization of MOFs and AuNPs. We have first synthesized a UiO-66-NH_2 nanoparticle, a typical Zr-MOF based on a previous report.[24] Then, to certify the interaction of AuNPs with the Zr-MOF, images of the Zr-MOF, AuNPs, AuNPs + Zr-MOF, and ssDNA-AuNPs + Zr-MOF complex are characterized by transmission electron microscopy (TEM) imaging and powder X-ray diffraction (PXRD) patterns. These results indicate that MOFs have intact crystal morphology with a size of approximately 100 nm (Figures 1A and S1). Figure 1B shows that the synthesized AuNPs have a uniform size of around 15 nm. From Figure 1C,D, it is observed that only ssDNA-modified AuNPs can be absorbed by Zr-MOFs, while bare AuNPs are hardly bound to Zr-MOFs, which indicates that ssDNA plays an important role in their integration.

UV−vis spectroscopy has also been used to demonstrate the specific interaction between the ssDNA−AuNPs and Zr-MOF. Figure S2 shows the 15 nm AuNPs with a typical maximum absorbance of 521 nm, which is almost the same after being mixed with the Zr-MOF. The absorption peak of ssDNA-AuNPs is 525 nm, which has a slight red shift compared with plain AuNPs, because of the size-dependent surface plasmon resonance absorption. Moreover, ssDNA-AuNPs have a significant absorption peak enhancement at 260 nm, which proves the success of connection between DNA and AuNPs. However, after incubating with the Zr-MOF, the absorbance in the supernatant significantly decreases and becomes almost 0. The binding of ssDNA to AuNPs has also been confirmed by agarose gel electrophoresis (Figure S3). These results

DOI: 10.1021/acsami.9b10729
ACS Appl. Mater. Interfaces 2019, 11, 36316−36323

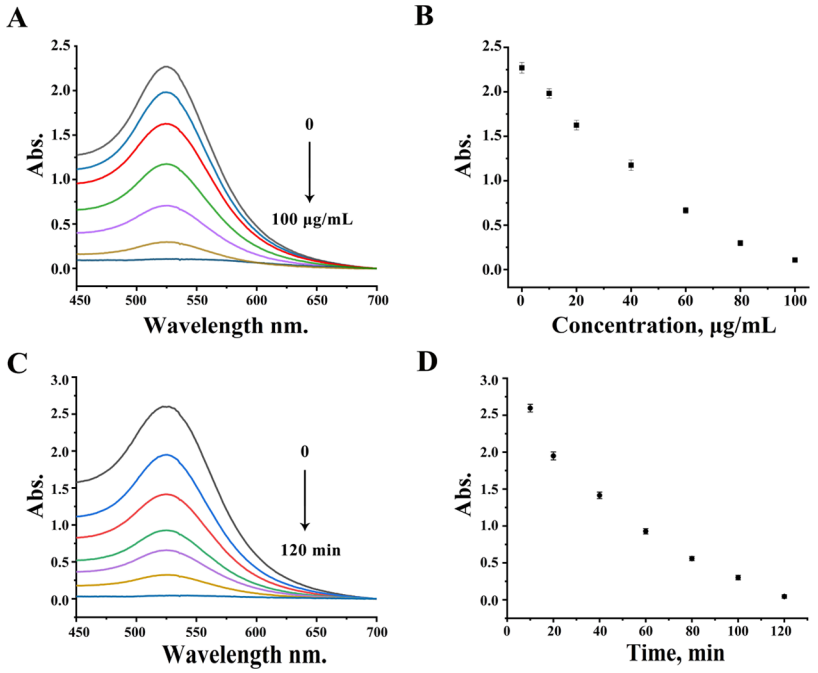

Figure 2. (A) Absorbance of ssDNA−AuNPs incubated with different concentrations (0, 10, 20, 40, 60, 80, and 100 μg/mL) of Zr-MOF. (B) The relationship between the peak absorbance and different concentrations of Zr-MOF. (C) The absorbance of ssDNA−AuNPs mixed with Zr-MOF for 2 h; the spectra are recorded at time intervals of 20 min from 0 to 120 min. (D) The relationship between the peak absorbance and different incubation times. Error bars are obtained from three parallel experiments.

demonstrate that Zr-MOFs have the ability to adsorb onto and precipitate ssDNA-AuNPs, resulting in a reduction in absorbance for the test solution.

3.2. Optimization of Experimental Conditions. To achieve a better performance of the sensor array, the experimental parameters have been optimized. Since the sensor array relies on the diverse interactions between Zr-MOF and ssDNA-AuNPs as well as proteins, the Zr-MOF concentration is optimized at first. Different concentrations of Zr-MOF have been employed to interact with ssDNA-AuNPs for 2 h, and the UV−vis spectra are recorded (Figure 2A). The maximum absorption values at 525 nm are picked to draw its corresponding curve. From Figure 2B, it can be known that the color intensity almost trends to zero when the Zr-MOF concentration reaches 100 μg/mL, indicating that the Zr-MOF at a concentration of 100 μg/mL can precipitate all ssDNA-AuNPs. Thus, the following experiments are carried out by using the Zr-MOF concentration of 100 μg/mL. Figure 2C indicates the UV−vis spectra of ssDNA-AuNP solution incubated with 100 μg/mL of Zr-MOF for different times. The dynamics curve of incubation at different times is plotted at the absorption values at 525 nm (Figure 2D). These results indicate that nearly all ssDNA-AuNPs can be bound and settled by Zr-MOF after incubating for 2 h. Thus, 2 h has been chosen as the optimal incubation time.

3.3. Sensor Array Responses to Proteins. After the experimental conditions have been optimized, six ssDNA-sequence-modified AuNPs (NP1−NP6, Table S1) are prepared as sensor elements and 10 different kinds of proteins are used as targets (Table S2) to investigate the feasibility of the colorimetric sensing array for the identification of human semen. Since the binding affinity between ssDNA and Zr-MOF sensitively depends on different nucleotides and sequences,[20] ssDNA sequences with different bases (poly-15A, -15T, -15C) and lengths (poly-5A, -15A) are designed. Meanwhile, selected proteins are employed, which differ in molecular weight (MW), isoelectric point (pI), and metal-containing center. For example, HRP is similar to Thr in MW but not in pI, Thr and Hem share a like pI but the MW is distinct. So, the proteins can bind with ssDNA-AuNPs and Zr-MOF with various forces and are easy to distinguish by generating differential colorimetric responses. When 20 μL of proteins (all at 0.5 nM) mixed with 60 μL of ssDNA-AuNPs are incubated for 30 min, the color of the test solution has hardly changed (Figure 3A). This demonstrates that the protein itself will not interfere with the stability of nanoparticles. However, there are a variety of colorimetric responses after further incubation of the above test solution with 30 μL of Zr-MOF, suggesting that different proteins may have different effects on the cross-linking between the ssDNA-AuNPs and Zr-MOF (Figure 3B).

The changes of absorbance before and after adding proteins in the test solution have been recorded in the training matrix ($\Delta A = A_0 - A$). Each experiment has been repeated six times. Different absorbance responses can be obtained from different proteins by using different sensing elements, indicating that each protein has a unique effect on the nanoparticles (Figure 4A). This is because the specific adsorption of protein on the ssDNA-AuNP or Zr-MOF surface will hinder the cross-linking between them. To clearly show the fingerprint response patterns of each protein, we have converted the color change of the absorbance pattern to a heat map (Figure 4B). This apparent discrimination proves that the sensing array can successfully recognize different kinds of proteins.

To display the fingerprints more distinctly, the training matrix pattern (6 sensing elements × 10 proteins × 6 replicates) has been subjected to linear discriminant analysis (LDA), a statistical technique, which can maximize the ratio of between-class variance to within-class variance and show decent discrimination of the proteins[28] (Table S5). The raw data have been subjected to LDA and generate four canonical

DOI: 10.1021/acsami.9b10729
ACS Appl. Mater. Interfaces 2019, 11, 36316−36323

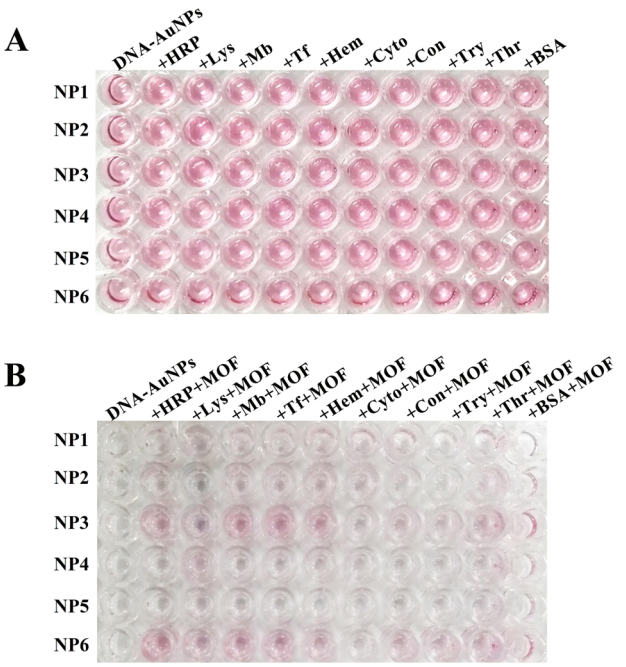

Figure 3. Colorimetric response pattern obtained from the different sensor elements (NP1−NP6) after the incubation of 10 kinds of proteins with (A) no Zr-MOF and (B) Zr-MOF for 2 h.

factors (78.6, 13.6, 6.7 and 1.1%), representing the linear combinations of the absorption response matrix (4 factors × 10 proteins × 6 replicates). The most significant two factors are employed to generate a two-dimensional (2D) plot, showing that all of the proteins can be successfully distinguished without any overlap in this sensing system (Figure 4C). What is more, the metal-containing proteins, HRP, Tf, Mb, Hem, and Thr, are classified in the right quadrant. Proteins with a pI value higher than 7.4, such as Lys, Cyto and Try, are located in the other quadrant and are well differentiated. Proteins with similar MW or pI, such as HRP and Thr, Lys and Cyto, Try and Cyto, HRP and Con, can also be distinguished each other.[29] These results indicate that our sensor array can identify different proteins through the very subtle differences by LDA, which proves the efficiency of our strategy.

To evaluate that our assay can be applied in complex samples, human serum samples spiked with proteins have been measured (final protein concentration, each at 0.5 nM). Although the identification of protein in serum is more challenging than in buffers, our system can accurately identify nine proteins in serum and achieve 100% identification accuracy by LDA analysis. Five canonical factors (80.3, 12.9, 4.5, 1.4, and 0.9%) are generated and the 2D plot of the first two factors is presented in Figure 5C. Furthermore, unknown protein samples randomly selected from nine kinds of proteins are also detected to demonstrate the efficiency of our sensor array. Based on the typical predictive ability of LDA, we can detect which group the unknown sample belongs to.[28,30] Of the 25 samples, 24 proteins are correctly identified with an identification accuracy of 96% (Table S6). These results indicate that our strategy can efficiency identify different proteins without the influence of the complex composition in human serum.

3.4. Sensor Array Responses to Human Semen Samples. After successfully distinguishing proteins in real human serum samples, we have further applied the sensor array on the detection of male infertility, relying on the diversity of proteins in semen samples. First, we have collected clinical human semen samples from different cases, such as healthy, infertile, and recurrent abortion. To ensure heterogeneity and authenticity, seven patient samples are selected for each type. It is noted that the samples are diluted and directly used by the sensor array without any treatment. Specifically, 10 μL of the semen sample diluted with phosphate-buffered saline is incubated with 120 μL of ssDNA-AuNPs for 30 min. Then, 60 μL of Zr-MOFs are added in the mixture solution to conjugate and precipitate the remaining ssDNA-AuNPs or analytes. Each sample has been repeated six times, and the average value is recorded in the training matrix (Figure 6A). For the sake of clarity, the distinct fingerprint response patterns of three semen cases are converted to a heat map and LDA analysis is performed (Figure 6B). From the 2D plot with

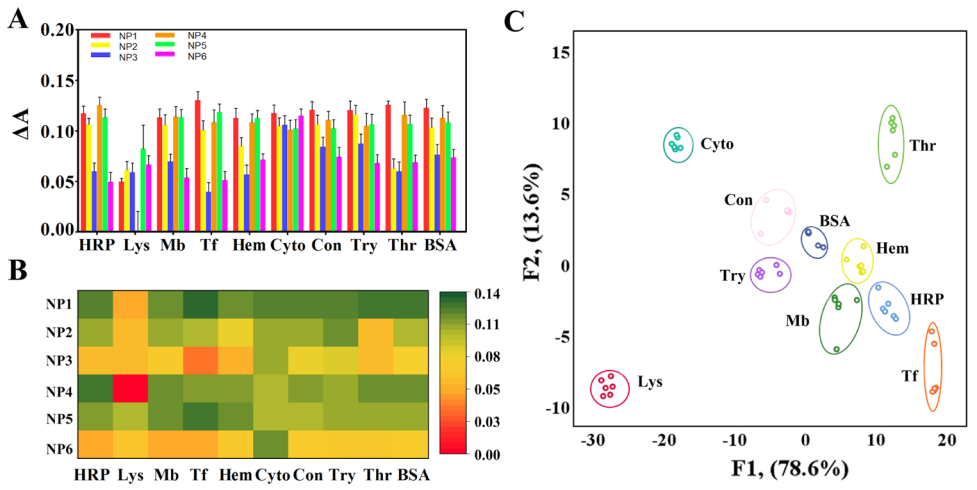

Figure 4. (A) Absorbance response pattern (ΔA, $A_0 - A$) obtained from the different sensor elements (NP1−NP6) against 10 proteins at 0.5 nM concentration in Tris−HCl (pH 7.4). Error bars represent standard deviations of six parallel measurements. (B) Heat map derived from the changes of the absorbance signal responses of NP1−NP6 against 10 proteins. (C) Canonical score plot using the first two factors obtained from the absorbance response pattern. Each point represents the response pattern for a single protein.

DOI: 10.1021/acsami.9b10729
ACS Appl. Mater. Interfaces 2019, 11, 36316−36323

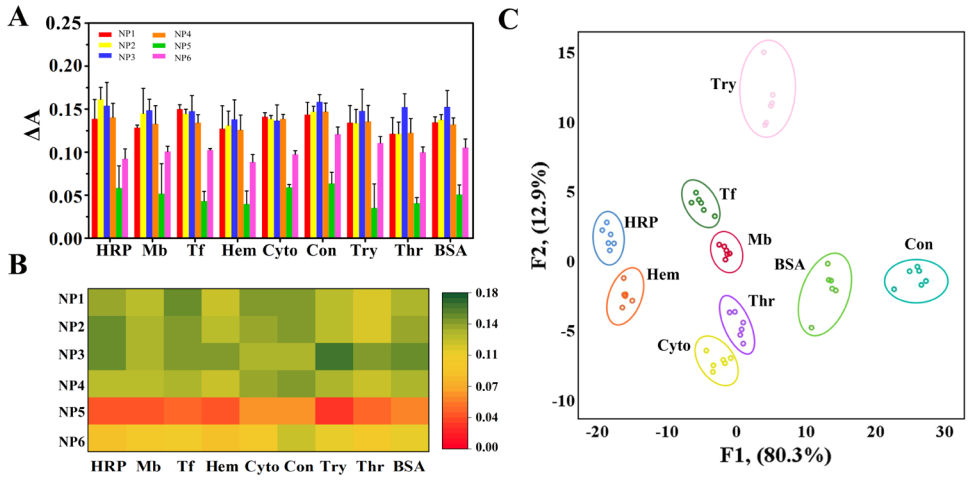

Figure 5. (A) Absorbance response pattern (ΔA, $A_0 - A$) obtained from the different sensor elements (NP1−NP6) against nine proteins at 0.5 nM concentration spiked in human serum. Error bars represent standard deviations of six parallel measurements. (B) Heat map derived from the changes of the absorbance signal responses of NP1−NP6 against nine proteins spiked in human serum. (C) Canonical score plot using the first two factors obtained from the absorbance response pattern. Each point represents the response pattern for a single protein in the human serum.

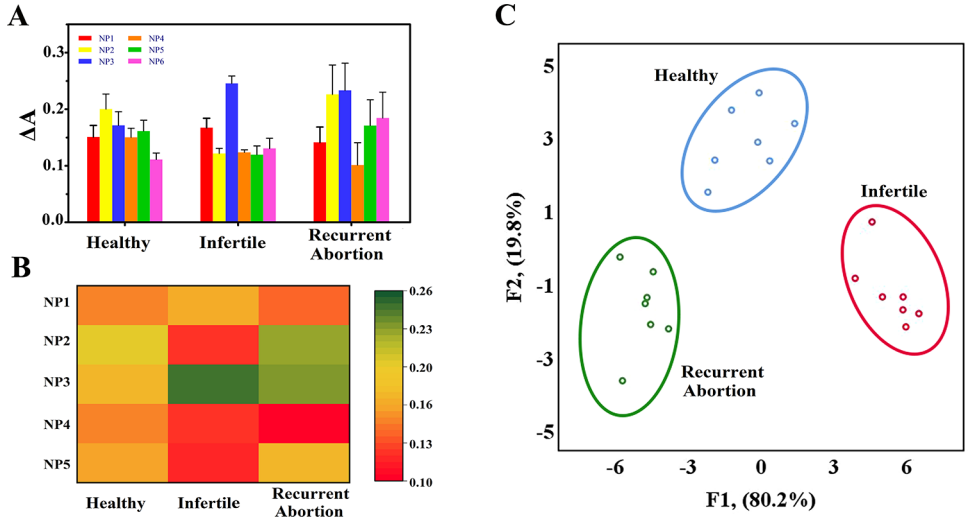

Figure 6. (A) Absorbance response pattern (ΔA, $A_0 - A$) obtained from the different sensor elements (NP1−NP6) against three different cases of semen samples. Error bars represent standard deviations of six parallel measurements. (B) Heat map derived from the absorbance response pattern for three different cases of semen samples. (C) Canonical score plot using the first two factors obtained from the absorbance response pattern. Each point represents the response pattern for a single semen species.

the two canonical factors (80.2 and 19.8%), we can clearly observe that the healthy semen samples are located on the upper side while infertility and recurrent abortion samples are located on the under side. Moreover, we have performed blind experiments to validate the efficiency of the sensor array. The unknown semen samples are randomly selected from cases that perform in our assay. Out of 20 cases, 18 are correctly classified with the identification accuracy of 90% (Table S8). These results demonstrate that our approach can easily and effectively identify healthy, infertile and recurrent abortion cases based on the distinct colorimetric patterns, which are produced by the coordination interactions between the Zr_6 clusters and the DNA phosphate backbone, as well as $\pi-\pi$ stacking and H-bonding. Moreover, since the interactions can be effectively affected by the various proteins in the semen sample, the system can be developed as a simple and useful discrimination tool to identify infertility in human semen samples, which may have a great prospective value for the medical diagnosis of male infertility.

4. CONCLUSIONS

In summary, we have proposed a colorimetric sensor array by coupling Zr-MOFs with ssDNA-AuNPs for rapid and accurate identification of human semen. In this system, six DNA-capped AuNPs act as the sensor elements. Since the sensor array can simultaneously detect different kinds of proteins by the relative absorption intensity variation, it can be used to explore the different types of male infertility. This work may provide a new method for the diagnosis of male infertility, and the method is simple, effective, cost-effective, and has great potential in POC testing. Moreover, this work may be further intended for use in the clinical examination of other diseases by coupling MOFs with AuNPs modified with other ssDNA sequences. Certainly, this method can only provide the information about the difference between the healthy, infertile, and recurrent

DOI: 10.1021/acsami.9b10729
ACS Appl. Mater. Interfaces 2019, 11, 36316−36323

abortion cases. It cannot give a quantitative analysis. Nevertheless, combined with appropriate devices for quantitative detection of specific targets, this method can be improved for further application in the future.

■ ASSOCIATED CONTENT

Supporting Information

The Supporting Information is available free of charge on the ACS Publications website at DOI: 10.1021/acsami.9b10729.

PXRD pattern of MOF; UV−vis spectroscopy of the AuNPs; oligonucleotide sequences; agarose gel electrophoresis of ssDNA-AuNPs; Jackknifed classification matrix; corresponding training matrix of absorbance response patterns (PDF)

■ AUTHOR INFORMATION

Corresponding Authors

*E-mail: lizhousun@yeah.net. Fax: +86-25-86663616 (L.S.).
*E-mail: genxili@nju.edu.cn. Fax: +86-25-83592510 (G.L.).

ORCID

Lizhou Sun: 0000-0002-1598-0828

Notes

The authors declare no competing financial interest.

■ ACKNOWLEDGMENTS

This work was supported by the National Natural Science Foundation of China (Grant no. 81772593).

■ REFERENCES

(1) Bracke, A.; Peeters, K.; Punjabi, U.; Hoogewijs, D.; Dewilde, S. A Search for Molecular Mechanisms Underlying Male Idiopathic Infertility. *Reprod. BioMed. Online* **2018**, *36*, 327−339.

(2) Agarwal, A.; Mulgund, A.; Hamada, A.; Chyatte, M. R. A Unique View on Male Infertility around the Globe. *Reprod. Biol. Endocrinol.* **2015**, *13*, No. 37.

(3) World Health Organization. *WHO Laboratory Manual for the Examination and Processing of Human Semen*; 5th ed.; WHO: Geneva, Switzerland, 2010.

(4) Cooper, T. G.; Noonan, E.; von Eckardstein, S.; Auger, J.; Baker, H. W.; Behre, H. M.; Haugen, T. B.; Kruger, T.; Wang, C.; Mbizvo, M. T.; Vogelsong, K. M. World Health Organization Reference Values for Human Semen Characteristics. *Hum. Reprod. Update* **2010**, *16*, 231−245.

(5) Jungwirth, A.; Giwercman, A.; Tournaye, H.; Diemer, T.; Kopa, Z.; Dohle, G.; Krausz, C. European Association of Urology Guidelines on Male Infertility: The 2012 Update. *Eur. Urol.* **2012**, *62*, 324−332.

(6) Jodar, M.; Soler-Ventura, A.; Oliva, R. Semen Proteomics and Male Infertility. *J. Proteomics* **2017**, *162*, 125−134.

(7) da Silva, B. F.; Meng, C.; Helm, D.; Pachl, F.; Schiller, J.; Ibrahim, E.; Lynne, C. M.; Brackett, N. L.; Bertolla, R. P.; Kuster, B. Towards Understanding Male Infertility after Spinal Cord Injury Using Quantitative Proteomics. *Mol. Cell. Proteomics* **2016**, *15*, 1424−1434.

(8) Druart, X.; Rickard, J. P.; Mactier, S.; Kohnke, P. L.; Kershaw-Young, C. M.; Bathgate, R.; Gibb, Z.; Crossett, B.; Tsikis, G.; Labas, V.; Harichaux, G.; Grupen, C. G.; de Graaf, S. P. Proteomic Characterization and Cross Species Comparison of Mammalian Seminal Plasma. *J. Proteomics* **2013**, *91*, 13−22.

(9) Primakoff, P. Penetration, Adhesion, and Fusion in Mammalian Sperm-Egg Interaction. *Science* **2002**, *296*, 2183−2185.

(10) Carrell, D. T.; Aston, K. I.; Oliva, R.; Emery, B. R.; De Jonge, C. J. The "Omics" of Human Male Infertility: Integrating Big Data in a Systems Biology Approach. *Cell Tissue Res.* **2016**, *363*, 295−312.

(11) Amaral, A.; Paiva, C.; Attardo Parrinello, C.; Estanyol, J. M.; Ballesca, J. L.; Ramalho-Santos, J.; Oliva, R. Identification of Proteins Involved in Human Sperm Motility Using High-Throughput Differential Proteomics. *J. Proteome Res.* **2014**, *13*, 5670−5684.

(12) Amaral, A.; Castillo, J.; Ramalho-Santos, J.; Oliva, R. The Combined Human Sperm Proteome: Cellular Pathways and Implications for Basic and Clinical Science. *Hum. Reprod. Update* **2014**, *20*, 40−62.

(13) Jodar, M.; Sendler, E.; Krawetz, S. A. The Protein and Transcript Profiles of Human Semen. *Cell Tissue Res.* **2016**, *363*, 85−96.

(14) Pepys, M. B.; Hirschfield, G. M.; Tennent, G. A.; Ruth Gallimore, J.; Kahan, M. C.; Bellotti, V.; Hawkins, P. N.; Myers, R. M.; Smith, M. D.; Polara, A.; Cobb, A. J. A.; Ley, S. V.; Andrew Aquilina, J.; Robinson, C. V.; Sharif, I.; Gray, G. A.; Sabin, C. A.; Jenvey, M. C.; Kolstoe, S. E.; Thompson, D.; Wood, S. P. Targeting C-Reactive Protein for the Treatment of Cardiovascular Disease. *Nature* **2006**, *440*, 1217−1221.

(15) He, G.; Luo, W.; Li, P.; Remmers, C.; Netzer, W. J.; Hendrick, J.; Bettayeb, K.; Flajolet, M.; Gorelick, F.; Wennogle, L. P.; Greengard, P. Gamma-Secretase Activating Protein Is a Therapeutic Target for Alzheimer's Disease. *Nature* **2010**, *467*, 95−98.

(16) Bunz, U. H.; Rotello, V. M. Gold Nanoparticle-Fluorophore Complexes: Sensitive and Discerning "Noses" for Biosystems Sensing. *Angew. Chem., Int. Ed.* **2010**, *49*, 3268−3279.

(17) Clelland, C. T.; Risca, V.; Bancroft, C. Hiding Messages in DNA Microdots. *Nature* **1999**, *399*, 533−534.

(18) Yang, X.; Li, J.; Pei, H.; Li, D.; Zhao, Y.; Gao, J.; Lu, J.; Shi, J.; Fan, C.; Huang, Q. Pattern Recognition Analysis of Proteins Using DNA-Decorated Catalytic Gold Nanoparticles. *Small* **2013**, *9*, 2844−2849.

(19) Wang, S.; McGuirk, C. M.; Ross, M. B.; Wang, S.; Chen, P.; Xing, H.; Liu, Y.; Mirkin, C. A. General and Direct Method for Preparing Oligonucleotide-Functionalized Metal-Organic Framework Nanoparticles. *J. Am. Chem. Soc.* **2017**, *139*, 9827−9830.

(20) Wang, Z.; Fu, Y.; Kang, Z.; Liu, X.; Chen, N.; Wang, Q.; Tu, Y.; Wang, L.; Song, S.; Ling, D.; Song, H.; Kong, X.; Fan, C. Organelle-Specific Triggered Release of Immunostimulatory Oligonucleotides from Intrinsically Coordinated DNA-Metal-Organic Frameworks with Soluble Exoskeleton. *J. Am. Chem. Soc.* **2017**, *139*, 15784−15791.

(21) He, C.; Lu, K.; Liu, D.; Lin, W. Nanoscale Metal-Organic Frameworks for the Co-Delivery of Cisplatin and Pooled Sirnas to Enhance Therapeutic Efficacy in Drug-Resistant Ovarian Cancer Cells. *J. Am. Chem. Soc.* **2014**, *136*, 5181−5184.

(22) Wei, H.; Wang, Z.; Zhang, J.; House, S.; Gao, Y.-G.; Yang, L.; Robinson, H.; Tan, L. H.; Xing, H.; Hou, C.; Robertson, I. M.; Zuo, J.-M.; Lu, Y. Time-Dependent, Protein-Directed Growth of Gold Nanoparticles within a Single Crystal of Lysozyme. *Nat. Nanotechnol.* **2011**, *6*, 93−97.

(23) Monopoli, M. P.; Åberg, C.; Salvati, A.; Dawson, K. A. Biomolecular Coronas Provide the Biological Identity of Nanosized Materials. *Nat. Nanotechnol.* **2012**, *7*, 779−786.

(24) Schaate, A.; Roy, P.; Godt, A.; Lippke, J.; Waltz, F.; Wiebcke, M.; Behrens, P. Modulated Synthesis of Zr-Based Metal-Organic Frameworks: From Nano to Single Crystals. *Chem. - Eur. J.* **2011**, *17*, 6643−6651.

(25) FRENS, G. Controlled Nucleation for the Regulation of the Particle Size in Monodisperse Gold Suspensions. *Nat. Phys. Sci.* **1973**, *241*, 20−22.

(26) Jin, R.; Wu, G.; Li, Z.; Mirkin, C. A.; Schatz, G. C. What Controls the Melting Properties of DNA-Linked Gold Nanoparticle Assemblies? *J. Am. Chem. Soc.* **2003**, *125*, 1643−1654.

(27) Wei, M.; Chen, N.; Li, J.; Yin, M.; Liang, L.; He, Y.; Song, H.; Fan, C.; Huang, Q. Polyvalent Immunostimulatory Nanoagents with Self-Assembled Cpg Oligonucleotide-Conjugated Gold Nanoparticles. *Angew. Chem., Int. Ed.* **2012**, *51*, 1202−1206.

(28) Jurs, P. C.; Bakken, G. A.; McClelland, H. E. Computational Methods for the Analysis of Chemical Sensor Array Data from Volatile Analytes. *Chem. Rev.* **2000**, *100*, 2649−2678.

(29) You, C. C.; Miranda, O. R.; Gider, B.; Ghosh, P. S.; Kim, I. B.; Erdogan, B.; Krovi, S. A.; Bunz, U. H.; Rotello, V. M. Detection and

Identification of Proteins Using Nanoparticle-Fluorescent Polymer 'Chemical Nose' Sensors. *Nat. Nanotechnol.* **2007**, *2*, 318−323.
(30) Diehl, K. L.; Anslyn, E. V. Array Sensing Using Optical Methods for Detection of Chemical and Biological Hazards. *Chem. Soc. Rev.* **2013**, *42*, 8596−8611.

DOI: 10.1021/acsami.9b10729
ACS Appl. Mater. Interfaces 2019, 11, 36316−36323